DISTANCE ESTIMATION BASED ON LIGHT FIELD GEOMETRIC MODELING

Yanqin Chen, Xin Jin and Qionghai Dai

Shenzhen Key Lab of Broadband Network and Multimedia,
Graduate School at Shenzhen, Tsinghua University, Shenzhen 518055, China
jin.xin@sz.tsinghua.edu.cn

ABSTRACT

In this paper, geometric optical models are proposed that can accurately estimate the distances of object planes in a light field image. Treating an arbitrary point on an object plane as an off-axis point light source, the single-point-light-source model, which consists of two relaying models, is established to describe the propagation of light rays from the off-axis point light sources to the image sensor. Based on the relaying models, the distances of object planes can be estimated by deriving the relationship between the positions of light rays impinging on the image sensor and incident angles of light rays entering into the main lens. Furthermore, taking into account the realistic imaging, the so-called line-source model is established by extending the off-axis point light sources to general line sources. The performances of the proposed models are compared with existing distance estimation methods under two optical configurations of plenoptic 1.0 cameras and results demonstrate that the proposed methods improve estimation accuracy by an average of 2.315%/4.675% for point light sources and 2.77% for a line source.

Index Terms— Light field, distance estimation, off-axis point light source, relaying models, line source

1. INTRODUCTION

Light field imaging becomes increasingly attractive in a variety of applications [1-3]. Compared with other light field acquisition systems [4-6], microlens array (MLA) based hand-held light field cameras offer a cost-effective approach, and have been adopted into industry and consumer market, known as plenoptic 1.0 (Lytro) and 2.0 (Raytrix) cameras [7-8]. Different from traditional cameras, plenoptic cameras can capture both spatial and angular light information (using plenoptic 1.0 cameras as an instance in Fig.1), which enable new capabilities, such as refocusing [9], viewpoint synthesis [10], and extending the depth of field after capturing [11]. Currently, estimating the distances of object planes in an image captured by a plenoptic 1.0 camera is becoming another attractive topic to its applications.

Distance can be inversely calculated by utilizing the depth information estimated from the light field [12-13]. However, the depth maps are usually rough due to the narrow baseline and low spatial resolution of plenoptic 1.0 cameras, especially in texture-less regions. Thus, the accuracy is too limited. Hanne *et al.* [14] proposed a ray tracing method based on the imaging system of plenoptic 1.0 cameras, which can estimate the distances of object planes the user is refocusing. Nevertheless, the method is incapable to estimate the distances of all object planes through only one refocusing implementation. In order to solve this drawback and simultaneously provide higher estimation accuracy, Chen *et al.* [15] proposed a geometric optical model which estimates the distance by investigating its relationship with the imaging diameter. However, the model provided in [15] is derived on account of on-axis point light sources. Therefore, it is lack of generality and practicability.

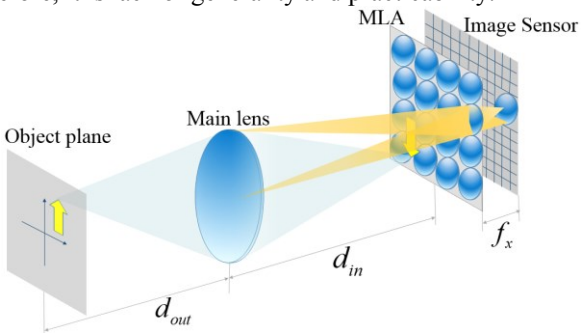

Fig.1. Plenoptic 1.0 cameras.

In this paper, we extend the work [15] by proposing the single-point-light-source model that supports locating the point light sources arbitrarily on the object planes. This model describes the propagation of light rays from the off-axis point light sources to the image sensor. Furthermore, considering that the realistic imaging is more complicated, the off-axis point light sources are extended to general line sources. Both the line-source geometric optical model and mathematical derivations are deduced to estimate the distances of object planes. Experiments are conducted under different optical configurations of plenoptic 1.0 cameras and results demonstrate that the proposed methods outperform existing distance estimation methods by an average of 2.315%/4.675% for point light sources and 2.77% for a line source. The improvement of estimation accuracy is obvious,

978-1-5386-0560-8/17/$31.00 ©2017 IEEE

especially at general imaging range.

The rest of the paper is organized as follows. Section 2 describes the geometric optical models in detail based on the optical analysis of single point light source imaging and a general line source imaging. Section 3 provides performance comparison and analyses. Conclusions are drawn in Section 4 as well as some potential future works.

2. GEOMETRIC OPTICAL MODELS

2.1. Optical Analysis

For an arbitrary point on the object plane, light rays emitting from the point can be considered as propagating from an off-axis point light source with an offset Δh, as shown in Fig.2. Thus, an on-axis source corresponds to $\Delta h = 0$. With the assumptions that light rays entering the main lens by covering its whole pupil diameter and refractions on MLA are neglected, imaging of a point light source varies with the distance of the plane which the point light source is located on, as depicted in Fig.2. As we can see from Fig.2, the imaging diameters on the image sensor are different and dependent on the defocuses of the object planes, i.e. a, $\tilde{\imath}$ and $\hat{a}$, which directly relates to the distance between the object plane and the main lens. This discovery implies that the distance of an object plane is possible to be estimated by investigating its association with the imaging diameter.

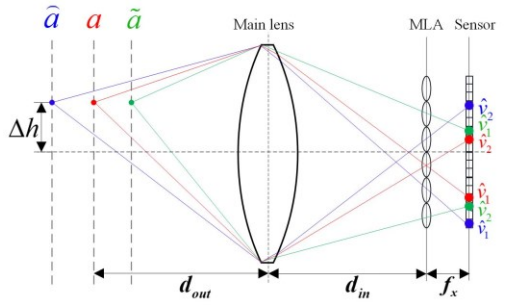

Fig.2. Imaging of off-axis point light sources at different distances. The offset apart from the optical axis is Δh.

2.2. Single-Point-Light-Source Geometric Optical Model

According to the above analysis, a single-point-light-source model is proposed, which consists of two relaying models, namely object space model and image space model.

Using plane $\tilde{\imath}$ in Fig.2 as an instance, the object space model is displayed in Fig.3. In this relaying model, light rays emitting from an off-axis point light source with offset being Δh, propagate into the main lens and refract inside it following refraction theorem. As shown in Fig.3, d_{out}' defines the distance between plane $\tilde{\imath}$ and the main lens, which is exactly needed to be estimated. Its relationship with the incident angle, denoted by φ_i in Fig.3, is mathematically given by

$$\tan\varphi_i = \frac{D/2 + (\mathrm{sgn}(i)\Delta h)}{(d_{out}' - T/2 + R - \sqrt{R^2 - D^2/4})}, \tag{1}$$

where R represents the radius of curvature of main lens; T represents the central thickness of main lens; D is the pupil diameter of main lens; $\mathrm{sgn}(i)$ is defined by

$$\mathrm{sgn}(i) = \begin{cases} -1 & i = 1 \\ 1 & i = 2 \end{cases}. \tag{2}$$

Eq.(1) indicates that Δh and d_{out}' can be obtained by calculating

$$\begin{aligned} \Delta h &= \frac{D(\tan\varphi_2 - \tan\varphi_1)}{2(\tan\varphi_2 + \tan\varphi_1)}, \\ d_{out}' &= \frac{D/2 + (\mathrm{sgn}(i)\Delta h)}{\tan\varphi_i} + \sqrt{R^2 - D^2/4} - R + T/2. \end{aligned} \tag{3}$$

Eq.(3) implies that φ_i is needed to be obtained in order to calculate Δh and further estimate d_{out}'.

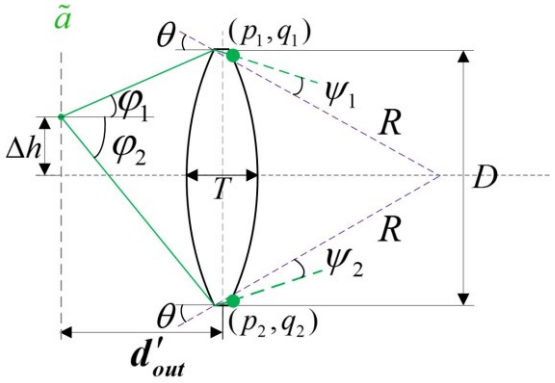

Fig.3. Object space model: light rays propagation from the point light source to the main lens.

After entering the main lens, light rays will refract inside the main lens and respectively arrive at (p_i, q_i), which is marked by green dot. The refractive angle, ψ_i, satisfies the refraction theorem, which is given by

$$n_1 \sin\psi_i = \sin(\varphi_i + \theta), \tag{4}$$

where n_1 is the refractive index of the main lens; ψ_i is the included angle between the normal (the dashed lines highlighted in purple) and the refractive light rays inside the main lens; θ follows

$$\sin\theta = \frac{D}{2R}. \tag{5}$$

After arriving at (p_i, q_i) as marked in Fig.3, light rays will exit from these positions with refractive angles ω_i, and then impinge on the image sensor. These propagations of light rays are carried out in the image space and the proposed image space model is shown in Fig.4.

By utilizing the refraction theorem again, it turns out that

$$n_1 \sin(\theta - \psi_i + \phi_i) = \sin\omega_i, \tag{6}$$

where ϕ_i follows

$$\sin\phi_i = \frac{|q_i|}{R}. \tag{7}$$

978-1-5090-6067-2/17/$31.00 ©2017 IEEE

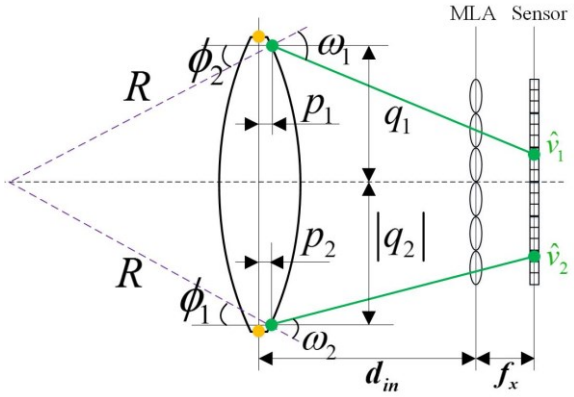

Fig.4. Image space model: light rays propagation from the main lens to the image sensor.

As the refractions on MLA are ignored, we have

$$\tan(\omega_i - \phi_i) = \frac{|q_i + (\mathrm{sgn}(i)\hat{v}_i)|}{f_x + d_{in} - p_i}, \tag{8}$$

where $\hat{v}_i$ represents the vertical coordinates and $|\hat{v}_1 - \hat{v}_2|$ equals to the imaging diameter of light rays on the image sensor; f_x is the focal length of MLA and d_{in} defines the distance between MLA and main lens. Besides, (p_i, q_i) lies on the curved surface of main lens so that p_i and q_i satisfy

$$(R - T/2 + p_i)^2 + q_i^2 = R^2, \tag{9}$$

Analyses on Eqs.(8) and (9) manifest that p_i and q_i can only be obtained after d_{in}, $\hat{v}_i$, and $\omega_i - \phi_i$ are all known.

In order to get the values of d_{in}, $\hat{v}_i$, refocusing and inverse ray tracing are required. Therefore, the light field image is refocused to a reference plane at a known distance away from the main lens once it is captured. The refocusing is implemented by using the synthesis technique proposed in [14] as shown in Fig.5. The reference plane can be identified as the plane a in Fig.2 whose distance is d_{out}. The method [14] traces a pair of light rays emitting from corresponding pixels on the image sensor back to the object space, and the intersection of light rays with the same color is taken as the distance of the refocused object plane. Therefore, the slopes of light rays in image space, m_k, and object space, s_{kj}, are required to be obtained, which are respectively given by

$$m_k = \frac{y_j - v_{kj}}{f_x}, \tag{10}$$

$$s_{kj} = \frac{y'_j - F_k}{d_{out} - f}, \tag{11}$$

where y_j represents the vertical central coordinates of each micro lens and v_{kj} represents the vertical central coordinates of each pixel on the image sensor; y'_j denotes the known vertical coordinates of calibrated points on plane a; f is the focal length of main lens; F_k denotes the interval between the intersections of corresponding light rays on plane F_u, and the intervals are the baselines of virtual viewpoints in hand-held plenoptic 1.0 cameras [14].

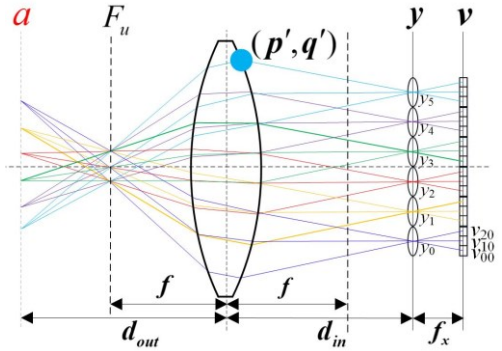

Fig.5. Refocusing model for deriving d_{in} where $\boldsymbol{y}$ and $\boldsymbol{v}$ represent MLA and image sensor, respectively.

Subsequently, the positions of light rays in object space intersecting on the main lens can be ascertained as well as corresponding positions (p', q'), as marked in Fig.5. Finally, d_{in} can be obtained by

$$d_{in} = \frac{q' - y_j + m_i p'}{m_i}. \tag{12}$$

$\hat{v}_i$ can then be achieved by recording the vertical coordinates of light rays that impinge on the image sensor, in the refocused light field image.

For the purpose of achieving the value of $\omega_i - \phi_i$, an approximation is made in the image space model that light rays will intersect at the yellow dots as marked in Fig.4, the centers of marginal pupil diameter of main lens, supposing the light rays are prolonged on the main lens. By combining Eq.(8) and utilizing similar triangle principle which gives

$$\frac{D/2 + (\mathrm{sgn}(i)\hat{v}_i)}{f_x + d_{in}} \approx \frac{|q_i + (\mathrm{sgn}(i)\hat{v}_i)|}{f_x + d_{in} - p_i}, \tag{13}$$

$\omega_i - \phi_i$ can then be approximately achieved by

$$\tan(\omega_i - \phi_i) \approx \frac{D/2 + (\mathrm{sgn}(i)\hat{v}_i)}{f_x + d_{in}}. \tag{14}$$

After the above processing and approximation, p_i and q_i can be derived by plugging d_{in}, $\hat{v}_i$, and $\omega_i - \phi_i$ into Eqs.(8) and (9), which is used for deriving d'_{out}.

After that, refractive angle ω_i can be calculated by

$$\omega_i = \arctan\left(\frac{|q_i + (\mathrm{sgn}(i)\hat{v}_i)|}{f_x + d_{in} - p_i}\right) + \arcsin\left(\frac{|q_i|}{R}\right). \tag{15}$$

Subsequently, ψ_i and φ_i can be obtained by solving

$$\psi_i = \arcsin\left(\frac{D}{2R}\right) + \arcsin\left(\frac{|q_i|}{R}\right) - \arcsin(\sin(\omega_i)/n_1), \tag{16}$$

$$\varphi_i = \arcsin(n_1 \sin(\psi_i)) - \arcsin\left(\frac{D}{2R}\right). \tag{17}$$

978-1-5090-6067-2/17/$31.00 ©2017 IEEE

Finally, d'_{out} can be obtained by plugging the calculated φ_i into Eq.(3).

For plane $\hat{a}$ in Fig.2, its object space model is the same as Fig.3 shows. Difference exists in the image space model since currently the focal plane in image space is located between the main lens and MLA. However, deriving the distance of plane $\hat{a}$ is exactly the same as plane $\tilde{a}$.

2.3. Line-Source Geometric Optical Model

Considering that the realistic imaging is more complicated, the above model derived based on an off-axis point light source is extended to a general line source. A line source can be regarded as a combination of infinite point light sources. For the ith point light source on the line, Eq.(3) indicates that

$$D/2-\Delta h_i = d\tan\varphi_{i1}, \qquad i\in[1,n] \tag{18}$$

where $d = d'_{out} - \sqrt{R^2 - D^2/4} - R + T/2$ and φ_{i1} denotes the angle φ_1 of the ith point light source. Note that φ_{i2} can also be used to derive an equation like (18) while $D/2-\Delta h_i$ should be replaced by $D/2+\Delta h_i$. Therefore, we have

$$\begin{aligned} d_i &\approx \frac{\Delta h_1 - \Delta h_2}{\tan\varphi_{21} - \tan\varphi_{11}} \approx \cdots \approx \frac{\Delta h_{i-1} - \Delta h_i}{\tan\varphi_{i1} - \tan\varphi_{(i-1)1}} \\ &\approx \cdots \approx \frac{\Delta h_{n-1} - \Delta h_n}{\tan\varphi_{n1} - \tan\varphi_{(n-1)1}}, \end{aligned} \tag{19}$$

which means

$$d_i \approx \frac{\Delta h_1 - \Delta h_n}{\tan\varphi_{n1} - \tan\varphi_{11}}, \qquad i\in[1,n]. \tag{20}$$

Eq.(20) demonstrates that for a line source, the distance between the plane, where the line source is located, and the main lens can be estimated by using the imaging information of two endpoints of the line source. It is applicable since the imaging diameter of a line source inherently is determined by the two endpoints of the line source, as shown in Fig.6.

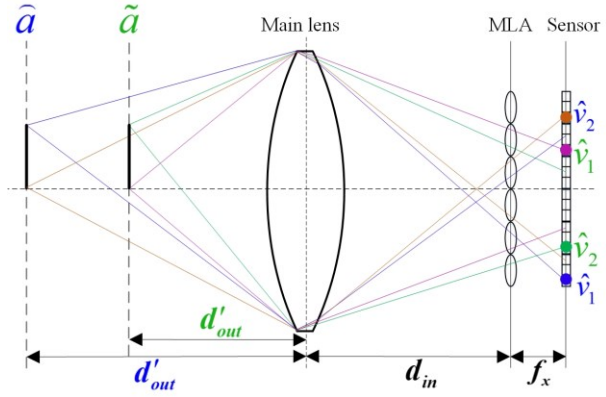

Fig.6. Imaging of line sources at different distances.

Utilizing the fact that the imaging diameter of a point light source on the same object plane is almost the same, $\hat{v}_1$ and $\hat{v}_2$ for two endpoint light sources in Fig.6 can be obtained, respectively. After that, Δh_1 and Δh_n can be estimated using the derivations described in Section 2.2 and the distance of the object plane can be estimated using Eq.(20).

3. PERFORMANCE COMPARISON AND ANALYSES

3.1. Simulation System

In order to validate the effectiveness of the proposed geometric optical models, imaging systems of hand-held plenoptic 1.0 cameras are simulated in optics tool Zemax [16], as shown in Fig.7. The gap between the image sensor and MLA is magnified for better visibility. The performances of the proposed models are compared with the method provided in [14]. Two general optical settings of plenoptic 1.0 cameras designed in [14] and [17] are used for the simulated system **1** and **2**, respectively. The optical parameters of each system are listed in Table.1. The parameters of main lens in system **2** are changed a bit to keep its $F-number$ being equal to that of the MLA.

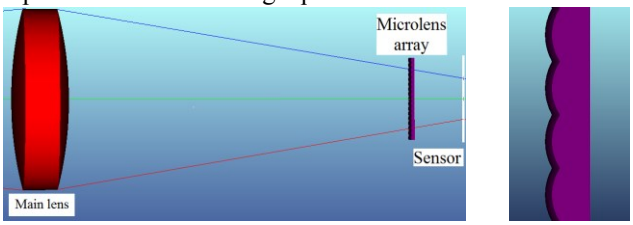

Fig.7. Zemax screenshots: (a) Simulated imaging system of hand-held plenoptic 1.0 cameras; (b) Zoomed MLA.

Table.1. Parameters of two simulated imaging systems.

Parameters	Imaging system **1**	Imaging system **2**
Focal length of each micro lens, f_x	**2.749mm**	**0.7mm**
Pitch size of each micro lens, D_m	**1.34mm**	**0.25mm**
Focal length of main lens, f	**99.515mm**	**98.088mm**
Pupil diameter of main lens, D	**50mm**	**40mm**
Central thickness of main lens, T	**14.35mm**	**6mm**
Radius of curvature of main lens, R	100mm	100mm
Refractive index of main lens, n_1	1.515	1.515
Wavelength of light rays, λ	632.8nm	632.8nm

3.2. Results and Analyses

The estimation error of distance, denoted by $ERROR$, is used for comparing the performances of the proposed models and the method in [14], which is given by

$$\begin{aligned} ERROR &= \frac{|d'_{out} - Ed'_{out}|}{d'_{out}} = \frac{|Ad + T/2 - (Ed + T/2)|}{Ad + T/2} \\ &= \frac{|Ad - Ed|}{Ad + T/2}, \end{aligned} \tag{21}$$

where d'_{out} represents the real distances of object planes, such as plane $\tilde{a}$ and $\hat{a}$, as depicted in Fig.2; Ed'_{out} denotes

978-1-5090-6067-2/17/$31.00 ©2017 IEEE

the estimated distances of object planes that are achieved according to the derivations in Section 2; *Ad* refers to the actual distances between object planes and the vertex of right curved surface of main lens on the axis. Therefore, d'_{out} equals to *Ad+T/2*; *Ed* represents the estimated distances between object planes and the vertex of right curved surface of main lens on the axis, which means Ed'_{out} equals to *Ed+T/2*. Results of estimated distances and estimation errors using single point light source with different Δh in the two imaging systems are listed in Table.2. Note that estimating the distance using the method in [14] is not associated with Δh nor the type of light sources.

Table.2. Estimation error comparison for an off-axis point light source.

Ad (mm)	Imaging system **1**						Imaging system **2**					
	Estimated by [14]		Estimated by Prop.				Estimated by [14]		Estimated by Prop.			
			$\Delta h = 5mm$		$\Delta h = 10mm$				$\Delta h = 5mm$		$\Delta h = 10mm$	
	Ed (mm)	*ERROR* (%)	*Ed* (mm)	*ERROR* (%)	*Ed* (mm)	*ERROR* (%)	*Ed* (mm)	*ERROR* (%)	*Ed* (mm)	*ERROR* (%)	*Ed* (mm)	*ERROR* (%)
3500	3278.40	**6.32**	3149.08	10.01	3148.73	10.02	3238.94	7.45	3383.22	**3.33**	3382.22	**3.36**
3250	3020.35	**7.05**	2946.02	9.33	2946.01	9.33	3044.34	6.32	3136.43	**3.49**	3136.85	**3.48**
3000	2792.09	**6.91**	2752.41	8.23	2753.17	8.21	2795.43	6.81	2885.30	**3.82**	2909.81	**3.00**
2800	2596.75	**7.24**	2578.02	7.91	2599.98	7.13	2603.61	7.01	2730.92	**2.46**	2730.88	**2.47**
2500	2333.13	**6.66**	2325.02	6.98	2324.44	7.00	2323.22	7.06	2441.69	**2.33**	2428.21	**2.87**
2200	2047.86	6.89	2059.55	**6.36**	2060.70	**6.31**	2053.18	6.66	2155.13	**2.04**	2146.20	**2.44**
2000	1856.75	7.14	1881.27	**5.92**	1889.91	**5.48**	1866.26	6.68	1962.10	**1.89**	1954.38	**2.28**
1800	1665.32	7.45	1708.45	**5.07**	1709.02	**5.03**	1683.27	6.47	1768.30	**1.76**	1768.94	**1.72**
1500	1387.31	7.48	1434.96	**4.32**	1434.48	**4.35**	1400.86	6.60	1480.02	**1.33**	1480.45	**1.30**
1300	1203.42	7.39	1249.56	**3.86**	1253.00	**3.60**	1213.77	6.62	1283.74	**1.25**	1284.12	**1.22**
1100	1018.54	7.36	1062.35	**3.40**	1063.78	**3.27**	1027.82	6.54	1088.82	**1.01**	1088.80	**1.02**
900	833.74	7.30	874.48	**2.81**	874.75	**2.78**	841.95	6.43	893.22	**0.75**	892.96	**0.78**
750	695.43	7.21	732.27	**2.34**	732.23	**2.35**	703.48	6.18	745.34	**0.62**	745.34	**0.62**
600	557.19	7.05	588.40	**1.91**	588.93	**1.82**	563.27	6.09	597.37	**0.44**	597.39	**0.43**
450	419.22	6.73	443.59	**1.40**	443.63	**1.39**	424.00	5.74	448.98	**0.23**	449.00	**0.22**
300	281.76	5.94	297.77	**0.73**	297.76	**0.73**	284.78	5.02	300.28	**0.09**	300.28	**0.09**
Ave. (%)		7.30		**5.04**		**4.93**		6.48		**1.68**		**1.93**

Table.3. Estimation error comparison for a line source.

Ad (mm)	Estimated by [14]		Estimated by Prop.	
	Ed (mm)	*ERROR* (%)	*Ed* (mm)	*ERROR* (%)
3500	3278.40	**6.32**	3201.81	8.50
3250	3020.35	**7.05**	2968.67	8.64
3000	2792.09	**6.91**	2750.62	8.29
2800	2596.75	7.24	2597.23	**7.22**
2500	2333.13	6.66	2334.06	**6.62**
2200	2047.86	6.89	2083.81	**5.26**
2000	1856.75	7.14	1898.24	**5.07**
1800	1665.32	7.45	1711.75	**4.88**
1500	1387.31	7.48	1438.22	**4.10**
1300	1203.42	7.39	1248.39	**3.95**
1100	1018.54	7.36	1069.18	**2.78**
900	833.74	7.30	876.32	**2.61**
750	695.43	7.21	734.69	**2.02**
600	557.19	7.05	591.84	**1.34**
450	419.22	6.73	445.80	**0.92**
300	281.76	5.94	300.94	**0.31**
Ave. (%)		7.30		**4.53**

As shown in Table.2, the proposed geometric optical model outperforms the method in [14] for the majority of distances in imaging system **1** and the whole distance range in imaging system **2**. In addition, the proposed model is superior to the method [14] by an average of 2.26%/2.37% reduction in estimation error as $\Delta h = 5mm$ / $\Delta h = 10mm$ in imaging system **1**. In imaging system **2**, the average of estimation error reduces almost 3 times, and the maximum reduction reaches 55 times at 0.3m, which implies high potential of the proposed model in applications. It is also found that the obtained estimation errors of the two imaging systems are different, which indicates that the optical parameters of plenoptic 1.0 cameras can influence the estimation accuracy. The effects of changing parameters are under investigations as one of our future works.

Results of estimated distances and estimation errors using a 10mm line source in imaging system **1** are listed in Table.3. Results show that the proposed model can provide obvious improvement in the estimation accuracy, an average of 2.77% reduction compared with that of [14], at most of the distances, which demonstrates the effectiveness of the generalization.

The estimation error results listed in Table.2 and Table.3 are graphed in Fig.8. It is observed that the performances of the proposed models are lightly worse than [14] at quite farther distances in imaging system **1**. As pointed out in [15], the reason mainly lies in the approximation made in the image space model. During deriving Eq.(14), light rays r_1 and r_2 are respectively approximated by r_1' and r_2', as shown in Fig.9. Thus, deviations exist in the light rays emission position (p_i, q_i) on the main lens, which leads to the estimation errors. Farther distances on the object space generally cause larger Δq_i and finally result in larger

978-1-5090-6067-2/17/$31.00 ©2017 IEEE

estimation errors. However, the errors can be compensated by changing the parameters of plenoptic 1.0 cameras, as referred to the results of the two imaging systems in Table.2.

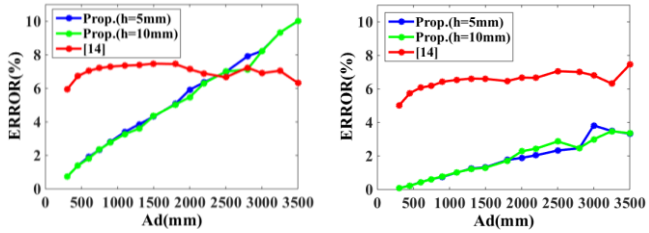

(a) Results of imaging system **1** in Table.2

(b) Results of imaging system **2** in Table.2

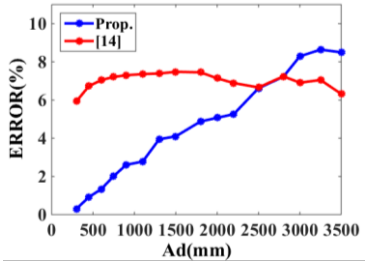

(c) Results of the line source in Table.3

Fig.8. Estimation error comparison.

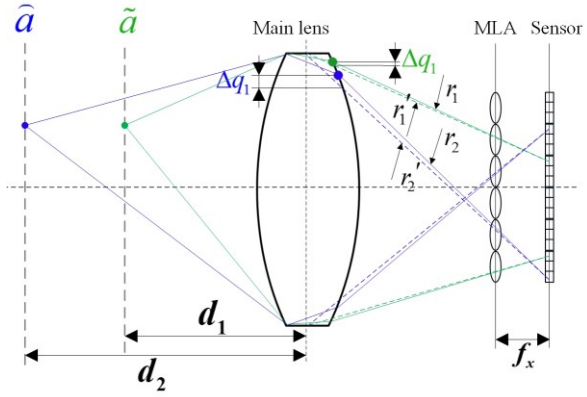

Fig.9. Ray tracing model for estimation error analysis.

4. CONCLUSIONS

In this paper, geometric optical models are put forward to estimate the distances of object planes in a light field image. Experimental results demonstrate that the proposed models can outperform existing distance estimation methods in terms of accuracy, particularly in general imaging range. We plan to build a real imaging system to verify the effectiveness of the proposed models while some problems need to be considered. For example, the noises, like calibration errors, should be compensated by introducing some correction factors into the proposed models. Besides, a simple thin lens is actually used in the proposed models for the sake of light weight and low cost of the plenoptic camera whereas includes optical aberrations, so it is important for us to correct the aberrations to restore light field images with high quality. We also imagine to extend the work to more areas, such as underwater imaging and microscopy.

5. ACKNOWLEDGEMENT

This work was supported in part by NSFC project of Guangdong 2014A030313733, the project of NSFC 61371138, and National Key Scientific Instrument and Equipment Development Project (NO.2013YQ140517), China.

6. REFERENCES

[1] Levoy M, Hanrahan P, "Light field rendering," In: ACM Int. Conf. on Computer Graphics and Interactive Techniques, pp. 1-8, Aug. 1996.

[2] Levoy M, Ng R, Adam A, Footer M, Horowitz M, "Light field microscopy," in *ACM Transactions on Graphics* (TOG), vol. 25, pp. 924-934, Jul. 2006.

[3] Fengchun D, Sio-Hoi I, Xavier S, Ralph Etienne C, and Ryad B, "Plenoptic cameras in real-time robotics," *The International Journal of Robotics Research*, vol. 32, pp. 206-217, Feb. 2013.

[4] Unger J, Wenger A, Hawkins T, Gardner A, Debevec P, "Capturing and rendering with incident light fields," In: Eurographics Workshop on Rendering, pp. 141–149, 2003.

[5] J C Yang, Everett M, Buehler C, McMillan L, "A real-time distributed light field camera," In: Eurographics Workshop on Rendering, pp. 77–86, Jun. 2002.

[6] Veeraraghavan A, Raskar R, Agrawal A, Mohan A, Tumblin J, "Dappled photography: mask enhanced cameras for heterodyned lightfields and coded aperture refocusing," In: ACM Transactions on Graphics (TOG), vol. 26, pp. 1–12, Jul. 2007.

[7] Lytro, inc. https://www.lytro.com/.

[8] Raytrix, gmbh. https://www.raytrix.de/.

[9] C Chen, Y Lu, and M Su, "Light field based digital refocusing using a DSLR camera with a pinhole array mask," 2010 *IEEE International Conference on Acoustics Speech and Signal Processing* (ICASSP), IEEE, pp. 754-757, 2010.

[10] Rematas K, Ritschel T, Fritz M and Tuytelaars T, "Image-Based Synthesis and Re-synthesis of Viewpoints Guided by 3D Models," 2014 *IEEE Conference on Computer Vision and Pattern Recognition* (CVPR), pp. 3898-3905, 2014.

[11] T.E. Bishop and P. Favaro, "The Light Field Camera: Extended Depth of Field, Aliasing, and Superresolution," 2012 IEEE Transactions on Pattern Analysis and Machine Intelligence (TPAMI), IEEE, pp. 972-986, 2012.

[12] M Tao, P Srinivasan, J Malik, S Rusinkiewicz and R Ramamoorthi, "Depth from shading, defocus, and correspondence using light-field angular coherence," in *Proceedings of IEEE Conference on Computer Vision and Pattern Recognition* (CVPR), pp. 1940-1948, 2015.

[13] H Jeon, J Park, G Choe, J Park, Y Bok, Y Tai, I Kweon, "Accurate depth map estimation from a lenslet light field camera," in *Proceedings of IEEE Conference on Computer Vision and Pattern Recognition* (CVPR), pp. 1547-1555, 2015.

[14] C Hahne, A Aggoun, V Velisavljevic, S Fiebig, and Matthias Pesch, "Refocusing distance of a standard plenoptic camera," Opt. Express 24, pp. 21521-21540, 2016.

[15] Y Chen, X Jin, Q Dai, "Distance measurement based on light field geometry and ray tracing," Opt. Express 25, pp. 59-76, 2017.

[16] "Zemax," http://www.zemax.com/.

[17] Georgiev T, Lumsdaine A, US Patent, "8400555", 2013.

978-1-5090-6067-2/17/$31.00 ©2017 IEEE